Scattering by Conducting Cylinders Below a Dielectric Layer With a Fast Noniterative Approach

Cristina Ponti, *Member, IEEE*, and Stefano Vellucci

***Abstract*—A spectral-domain technique to solve the scattering by perfectly conducting cylinders placed below a dielectric layer is presented. Propagation fields are expressed in an analytic form, in the frame of the cylindrical wave approach. The fields scattered by the buried objects are decomposed into cylindrical waves, which are, in turn, represented by plane-wave spectra. Due to the interaction with a layered layout, the scattered fields experience multiple infinite reflections at the boundaries of the layer. Using suitable reflection and transmission coefficients inside the plane-wave spectra, the interaction with such a layered geometry can be solved with a single-reflection approach. Multiple reflections are collected by a set of two scattered fields, i.e., an upward-propagating field, excited by the scatterers and transmitted up to the top medium, and a down-propagating one, which from the top medium reaches the scatterers after transmission through the layer. Therefore, the analytical theory is developed in a very compact way and can be solved through a fast and efficient numerical implementation. Numerical results are evaluated in an accurate way and validated by comparisons with results obtained with a multiple-reflection approach. The scattered field can be evaluated in any point of the domain, in the far-field as well as the near-field region. Two-dimensional maps displaying the magnitude of the total scattered field are reported, showing examples of applications of the technique.**

***Index Terms*—Electromagnetic simulation, full-wave analysis, scattering problems, spectral-domain technique, through-the-wall radar.**

I. Introduction

In recent years, a wide interest is arousing on the use of microwave electromagnetic fields for the nondestructive diagnostic of buried targets [1]. Practical applications are in the ground penetrating radar (GPR) technique, in the geophysical inspection of the soil, in the mapping of buried utilities, as well as in the surveys of roads, buildings, and bridges, and in the archeological field. The retrieval of the GPR data can be successfully improved using accurate electromagnetic solvers for the forward-scattering problem, to be used for the comparison of measured data with simulated ones, or to test new inversion algorithms. For an accurate modeling of the forward-scattering problem, several simulation parameters have to be taken into account, which are relevant to the source field, the scatterer, and the background medium. In many practical cases, a background with two semi-infinite media can be used for a modeling of the scattering problem, embedding the scatterers in the lowest half-space, and placing the source field in the top one. For the modeling of more complex scenarios, a more realistic description can be provided embedding the scatterers in a stratified geometry. Also the case of scatterers buried in a semi-infinite medium below a single layer or a multilayer is a useful model in the frame of civil engineering or geophysical applications, with the objects hidden by a road or a soil, respectively, as well as for through-wall scenarios [2], [3]. In the latter, targets are placed below a dielectric wall, in a semi-infinite medium filled by air, i.e., with same dielectric permittivity of the medium hosting the source of the scattering problem.

In the literature, a scattering solution is mainly developed with a target placed in a semi-infinite medium or inside a layer. A hybrid technique employing mode-matching method and finite-difference frequency-domain technique is developed in [4]–[6] to analyze scattering by cylindrical objects. In [7]–[11], cylinders are buried in a single layer between two half-spaces. A medium with an arbitrary number of planar dielectric layers embedding a perfectly conducting object of arbitrary shape is considered in [12] and [13], where a solution is developed with a mixed-potentials electric field integral equation, solved with the method of moments. Scattering by conducting cylinders in the presence of a stratified anystropic medium is solved in [14] using a combined Green's function and integral equation approach. The scattering problem of a target below a dielectric layer or a multilayer is mainly dealt with in the frame of through-wall applications. In particular, to assess performances achievable by an inversion algorithm for a through-wall imaging [15], scattered field by a cylinder below a wall is evaluated with GPRMAX2D, a free-of-charge software tool implementing the finite-difference time-domain (FDTD) method [16] to model GPR responses from arbitrarily complex targets. A general FDTD approach is also used in [17] to simulate ultra-wideband short-pulse radar for through-wall target detection. A hybrid FDTD technique and ray optics approximation are used for simulation of through-wall microwave imaging in [18]. A high-frequency ray-tracing approach is employed in [19] for electromagnetic characterization of building interior.

In [20], the scattering by perfectly conducting cylinders buried below a dielectric layer is solved in the frequency domain with the Cylindrical Wave Approach (CWA). CWA is an analytical-numerical method developed to solve scattering problems by cylindrical objects placed below planar or slightly rough boundaries [10], [11], [21]–[24]. In this approach, the scattered field is decomposed into cylindrical waves, which

Manuscript received July 17, 2014; revised October 02, 2014, November 23, 2014, and November 24, 2014; accepted November 25, 2014. Date of publication December 18, 2014; date of current version December 31, 2014. This paper is an expanded version from the IEEE MTT-S International Conference on Numerical Electromagnetic Modeling and Optimization for RF, Microwave, and Terahertz Applications, Pavia, Italy, May 14–16, 2014.

The authors are with the Department of Engineering, Roma Tre University, 00146 Rome, Italy (e-mail: cristina.ponti@uniroma3.it).

Color versions of one or more of the figures in this paper are available online at http://ieeexplore.ieee.org.

Digital Object Identifier 10.1109/TMTT.2014.2376553

are, in turn, expressed through a plane-wave spectrum in order to cope with reflection and transmission of the scattered field by the boundary. In the single-layer geometry used in [20], the scattering problem is solved implementing the CWA in a multiple-reflection approach.

This paper is an extension of the paper [24], where the scattering by a cylinder below a rough boundary was solved with the CWA. The general rules of the CWA implemented in [24] are applied to a scattering problem by buried cylinders in a layered background in order to extend the CWA to a wider class of scattering problems. In particular, the geometrical layout of scattering by cylinders below a dielectric layer analyzed in [20] is considered. In [20], reflection and transmission of the scattered fields through the layer was solved with an iterative approach. Infinite and convergent series of multiple-reflection fields were developed in the theoretical method. In the numerical implementation, such field contributions were evaluated in an iterative way up to the reach of convergence. The earlier approach [20] is now replaced by a more compact and efficient scattering theory with a noniterative scheme. In each medium, the scattered field is decomposed only in two field contributions, an upward-propagating and a downward-propagating one, respectively. The result of the multiple reflections inside the layer is described by the suitable reflection and transmission coefficients employed inside the spectral integrals used as basis functions of the scattered fields. In the frame of the spectral approach already used in [20] and [24], new cylindrical functions have been introduced in order to cope with two flat boundaries in an efficient way. Convergence of the new theory to the previous multiple-reflection approach in [20] is shown. Due to the low number of field contributions considered in the theoretical analysis, the theory can be solved through a faster code.

The numerical analysis is performed in an accurate way, following the integration algorithm employed in [24] for the spectral integrals. An accurate evaluation of such integrals allows to obtain results in far field as well as near field and zones. The three-media background used in the scattering problem is suitable for both an arbitrary scattering layout where the involved media have different permittivity, as well as in a through-wall problem, where the two external media are filled with air, whereas the central layer has an arbitrary relative permittivity. Numerical results show possible scenarios of applications, from geophysical to through-wall problems. In Section II, the theoretical approach is described. In Section III, numerical results are reported.

II. Theoretical Analysis

The geometry of the scattering problem is illustrated in Fig. 1. The top medium in the scattering layout (medium 0) is a half-space filled by air, i.e., with a vacuum-like permittivity ε_0. It is followed by a dielectric layer (medium 1) with permittivity $\varepsilon_1 = \varepsilon_0\varepsilon_{\mathrm{r}1}$, and a final half-space (medium 2) with permittivity $\varepsilon_2 = \varepsilon_0\varepsilon_{\mathrm{r}2}$. The involved dielectric media are linear, homogeneous, isotropic, and lossless and have vacuum magnetic permeability $\mu_2 = \mu_1 = \mu_0$. N perfectly conducting cylinders are embedded in medium 2, below the dielectric layer.

A main reference frame (MRF) (O, ξ, ζ) described by normalized coordinates $\xi = k_0 x$ and $\zeta = k_0 z$ is introduced, where $k_0 = \omega/c$ is the vacuum wavenumber. N reference frames $\mathrm{RF_p}$

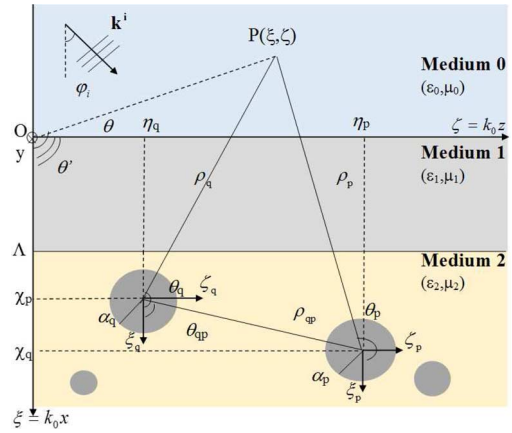

Fig. 1. Geometry of the problem.

centered on the axis of the p-th $(\mathrm{p} = 1, \ldots, N)$ cylinder are also used, both rectangular $(\mathrm{O_p}, \xi_\mathrm{p}, \zeta_\mathrm{p})$ and polar $(\mathrm{O_p}, \rho_\mathrm{p}, \theta_\mathrm{p})$, where $\xi_\mathrm{p} = k_0 x_\mathrm{p} = \xi - \chi_\mathrm{p}$, $\zeta_\mathrm{p} = k_0 z_\mathrm{p} = \zeta - \eta_\mathrm{p}$ and $\rho_\mathrm{p} = k_0 r_\mathrm{p}$. The dielectric layer is bounded by two flat interfaces located in $\xi = 0$ and $\xi = \Lambda$, in MRF. The pth cylinder has center in $(\chi_\mathrm{p}, \eta_\mathrm{p})$ in MRF and has normalized radius $\alpha_\mathrm{p} = k_0 a_\mathrm{p}$. A two-dimensional scattering problem is dealt with, as each cylinder has axis parallel to the y-direction, and the structure has infinite extension along the y-axis.

The source is a monochromatic plane wave of amplitude V_0, propagating in medium 0, and obliquely impinging on the interface between medium 0 and medium 1 in $\xi = 0$:

$$V_\mathrm{i}(\xi, \zeta) = V_0 e^{i(n^\mathrm{i}_\perp \xi + n^\mathrm{i}_\parallel \zeta)}. \tag{1}$$

The plane wave in (1) obliquely impinges on the separation interface in $\xi = 0$. It forms an angle φ_i with the ξ-axis, and its wavevector $\mathbf{k}_\mathrm{i}$ lies in the (ξ, ζ) plane. $n^\mathrm{i}_\perp$ and $n^\mathrm{i}_\parallel$ are the orthogonal and parallel components of $\mathbf{k^i}$, respectively; they are related to the incident angle through $k^\mathrm{i}_\perp = k_0 \cos\varphi_\mathrm{i}$ and $k^\mathrm{i}_\parallel = k_0 \sin\varphi_\mathrm{i}$. The time dependence of the field is $e^{-i\omega t}$, where ω is the angular frequency, and it is omitted throughout the paper.

The solution to the scattering problem is developed in terms of a scalar function $V(\xi, \zeta)$, representing the field component parallel to the y-direction: $V = E_y(\xi, \zeta)$ for TM-polarization, and $V = H_y(\xi, \zeta)$ for TE-polarization. In each medium, the function $V(\xi, \zeta)$ is expressed as the superposition of different field contributions, excited by the interaction of the source field with the interfaces and the cylinders. First, we distinguish plane-wave contributions. They propagate in the layered background of Fig. 2 and are evaluated in the absence of the cylinders, as follows:

- $V_\mathrm{i}(\xi, \zeta)$: plane-wave incident field, it is a downward-propagating wave in medium 0;
- $V_\mathrm{r}(\xi, \zeta)$: plane-wave reflected field, it is an upward-propagating wave in medium 0, excited by reflection of the incident field V_i by the layer;
- $V_{\mathrm{t}1}(\xi, \zeta)$: plane-wave transmitted field, it is a downward-propagating wave in medium 1, as the result of multiple reflections within the layer;
- $V_{\mathrm{r}1}(\xi, \zeta)$: plane-wave reflected field, it is an upward-propagating wave in medium 1, as the result of multiple reflections within the layer;

- $V_{\rm t2}(\xi,\zeta)$: plane-wave transmitted field, it is a downward-propagating wave in medium 2, due to the transmission of the incident field $V_{\rm i}$ beyond the layer.

The expressions of the plane-wave fields $V_{\rm r}$, $V_{\rm t1}$, $V_{\rm r1}$, and $V_{\rm t2}$ are [20]

$$V_{\rm r}(\xi,\zeta) = V_0\Gamma_{01}(n_{\parallel}^{\rm i})e^{{\rm i}\left(-{\rm n}_{\perp}^{\rm i}\xi+{\rm n}_{\parallel}^{\rm i}\zeta\right)} \tag{2}$$

$$V_{\rm t1}(\xi,\zeta) = V_0T_{01}\left(n_{\parallel}^{\rm i}\right)e^{in_1[n_{\perp}^{\rm t1}(\xi-\Lambda)+n_{\parallel}^{\rm t1}\zeta]} \tag{3}$$

$$V_{\rm r1}(\xi,\zeta) = V_0T_{01}\left(n_{\parallel}^{\rm i}\right)\Gamma_{12}\left(n_{\parallel}^{\rm i}\right)e^{in_1[-n_{\perp}^{\rm t1}(\xi-\Lambda)+n_{\parallel}^{\rm t1}\zeta]} \tag{4}$$

$$V_{\rm t2}(\xi,\zeta) = V_0T_{01}\left(n_{\parallel}^{\rm i}\right)T_{12}\left(n_{\parallel}^{\rm i}\right)e^{in_2[n_{\perp}^{\rm t2}(\xi-\Lambda)+n_{\parallel}^{\rm t2}\zeta]}. \tag{5}$$

Fields (2)–(5) are evaluated from the incident field through the reflection and transmission coefficients $\Gamma_{\rm rs}(n_{\parallel})$ and $T_{\rm rs}(n_{\parallel})$, respectively, relevant to a down-propagating plane wave in a layered medium [25]. Subscript s denotes the origin medium, whereas r stands for the medium of arrival, with $s = 0, 1$ and $r = 1, 2$. In (3), $n_{\perp}^{\rm t1} = n_{\parallel}^{\rm i}/n_1$ and $n_{\parallel}^{\rm t1} = \sqrt{1-(n_{\parallel}^{\rm i}/n_1)^2}$ are the orthogonal and parallel normalized components of the transmitted wavevector in medium 1, respectively, derived from Snell's law. In (5), the parallel and orthogonal components of the transmitted wavevector in medium 2 are $n_{\parallel}^{\rm t2} = n_1n_{\parallel}^{\rm t1}/n_2$ and $n_{\perp}^{\rm t2} = \sqrt{1-(n_1n_{\parallel}^{\rm t1}/n_2)^2}$, respectively. As the plane-wave field $V_{\rm t2}$ reaches the lowest medium, a set of scattered field is also excited. Symmetrically to what was done on the plane-wave fields, in each medium, the scattered field is decomposed only in two field contributions: an upward-propagating and a downward-propagating term, respectively. In particular, the following contributions can be distinguished [see Fig. 3]:

- $V_{\rm s}(\xi,\zeta)$: scattered field by the cylinders buried in medium 2;
- $V_{\rm sr}(\xi,\zeta)$: scattered-reflected field in medium 2 at the interface in $\xi = \Lambda$; it is a downward-propagating field after multiple reflections of the scattered field inside the layer;
- $V_{\rm st}^1(\xi,\zeta)$: scattered-transmitted field in medium 1 through the interface in $\xi = \Lambda$; it is an upward-propagating field after multiple reflections of the scattered field within the layer;
- $V_{\rm sr}^1(\xi,\zeta)$: scattered-reflected field in medium 1 at the interface in $\xi = 0$; it is a downward-propagating wave after multiple reflections of the scattered field within the layer;
- $V_{\rm st}^0(\xi,\zeta)$: scattered-transmitted field in medium 0; it is an upward-propagating field transmitted in the top medium after multiple reflections of the scattered field within the layer.

In this analytical approach, the scattered fields are written as a superposition of cylindrical waves through unknown coefficients. As the fields $V_{\rm sr}$, $V_{\rm st}^1$, $V_{\rm sr}^1$, and $V_{\rm st}^0$ are excited from reflection and transmission of the scattered field $V_{\rm s}$ by the interfaces, their analytical expressions are found expanding each cylindrical wave into a plane-wave spectrum, and evaluating for each plane wave the reflection and transmission through the layer. At this aim, the reflection and transmission coefficients $\Gamma_{\rm rs}(n_{\parallel})$ and $T_{\rm rs}(n_{\parallel})$ already used to define the plane-wave fields are applied to the scattered field contributions, inside the spectral integral. With respect to the previous case, the coefficients $\Gamma_{\rm rs}(n_{\parallel})$ and $T_{\rm rs}(n_{\parallel})$ are relevant to an upward-propagating wave, from medium 2 to medium 0, and they are used inside a spectral integral. Therefore, the direct expression of cylindrical wave interacting with a layered geometry is derived, avoiding to recur to a multiple-reflection scheme.

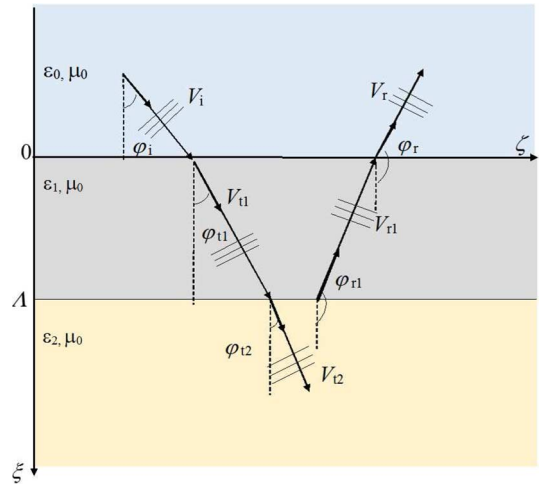

Fig. 2. Decomposition of the plane-wave fields.

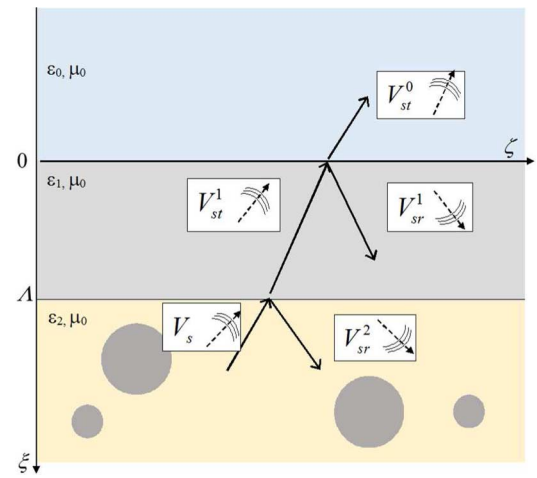

Fig. 3. Decomposition of the scattered fields.

A scattered field $V_{\rm s}$ is excited in medium 2: it is expressed as the sum of the fields scattered in medium 2 by each cylinder, written as a superposition of cylindrical functions ${\rm CW_m}(n_2\xi_{\rm q}, n_2\zeta_{\rm q})$, with unknown expansion coefficients $c_{\rm qm}$ [20], [21]:

$$V_{\rm s}(\xi,\zeta) = V_0\sum_{\rm q=1}^{N}\sum_{\rm m=-\infty}^{+\infty} c_{\rm qm}{\rm CW_m}(n_2\xi_{\rm q}, n_2\zeta_{\rm q}). \tag{6}$$

In (6), ${\rm CW_m}(n_2\xi_{\rm p}, n_2\zeta_{\rm p}) = H_{\rm m}^{(1)}(n_2\rho_{\rm p})e^{{\rm im}\theta_{\rm p}}$, where $H_{\rm m}^{(1)}$ is the first-kind Hankel function of integer order m, whereas p represents the pth cylinder.

The scattered field $V_{\rm s}$ (6) impinges on the lowest interface bounding the dielectric layer in $\xi = \Lambda$, exciting a downward-reflected wave in medium 2, i.e., the scattered-reflected field $V_{\rm sr}$, and upward-transmitted wave in medium 1, the scattered-transmitted field $V_{\rm st}$. Such field contributions are expanded into cylindrical waves as well by means of the same expansion coefficients $c_{\rm qm}$ used in (6). In particular, to express the fields $V_{\rm sr}$

and $V_{\rm st}$, the flat interface in $\xi = \Lambda$ is taken into account evaluating the reflection and transmission of each elementary plane wave constituting the Fourier spectrum of the cylindrical function $\mathrm{CW_m}$, employed in (6) to expand the scattered field. In particular, this is accomplished using as an alternative expression of the cylindrical waves $\mathrm{CW_m}$ the plane-wave spectrum [21], as follows:

$$\mathrm{CW_m}(\xi,\zeta) = \frac{1}{2\pi}\int_{-\infty}^{+\infty} F_{\rm m}(\xi, n_\parallel) e^{in_\parallel \zeta} dn_\parallel. \tag{7}$$

In (7), $F_{\rm m}$ represents the Fourier spectrum, defined as

$$F_{\rm m}(\xi, n_\parallel) = \frac{2}{\sqrt{1-(n_\parallel)^2}} e^{i|\xi|\sqrt{1-(n_\parallel)^2}} \times \begin{cases} e^{i\mathrm{m}\arccos n_\parallel}, & \xi \geq 0 \\ e^{-i\mathrm{m}\arccos n_\parallel}, & \xi \leq 0 \end{cases} \tag{8}$$

with $n_\parallel$ and $n_\perp = \sqrt{1-(n_\parallel)^2}$ being the parallel and orthogonal components of the normalized wavevector $\mathbf{n} = \mathbf{k}/k_0$ relevant to each plane wave of the spectrum, respectively.

In medium 2, the interaction of the scattered field with the upper layer excites a scattered-reflected field $V_{\rm sr}$. To express such a field, reflected cylindrical functions [21] are used as basis functions, evaluating reflection in medium 2 on each plane wave of the spectrum in (7), as follows:

$$\mathrm{RW_m}(\xi,\zeta) = \frac{1}{2\pi}\int_{-\infty}^{+\infty} \Gamma_{21}(n_\parallel) F_{\rm m}(\xi, n_\parallel) e^{in_\parallel \zeta} dn_\parallel \tag{9}$$

where the normalized reflection wavevector, derived from Snell's law, is $n^{\rm r} = -n_\perp \hat{\mathbf{x}} + n_\parallel \hat{\mathbf{z}}$. In (9), $\Gamma_{21}(n_\parallel)$ is the reflection coefficient, relevant to the interface of separation between medium 2 and medium 1 in $\xi = \Lambda$. It is noteworthy that, with respect to the definition of the reflected cylindrical waves given in [20], such functions do not deal only with reflection at the interface between medium 2 and medium 1, as the used reflection coefficient $\Gamma_{21}(n_\parallel)$ has a different definition, being relevant to a down-propagating wave, reflected in medium 2 at the bottom interface in $\xi = \Lambda$, after a convergent number of multiple reflections within the layer above [25]. Using the basis functions (9), the scattered-reflected field is

$$V_{\rm sr}(\xi,\zeta) = V_0 \sum_{\rm q=1}^{N} \sum_{\rm m=-\infty}^{+\infty} c_{\rm qm} \times \mathrm{RW_{m+\ell}}[-n_2(\xi + \chi_{\rm q} - 2\Lambda), n_2(\zeta - \eta_{\rm q})]. \tag{10}$$

As to the scattered-transmitted field $V_{\rm st}^1$ in medium 1, it is expressed in a similar manner through an expansion into transmitted cylindrical functions [21] relevant to propagation in medium 1:

$$\mathrm{TW_m^1}(\xi,\zeta;\chi) = \frac{1}{2\pi}\int_{-\infty}^{+\infty} T_{21}(n_\parallel) F_{\rm m}[-n_2(\chi_{\rm q} - \Lambda), n_\parallel] \times e^{in_1\sqrt{1-(n_2 n_\parallel/n_1)^2}(\xi-\Lambda)} e^{in_2 n_\parallel(\zeta-\eta_{\rm q})} dn_\parallel. \tag{11}$$

The $\mathrm{TW_m^1}$ in (11) is found evaluating transmission on each plane wave of the spectrum in (7). $T_{21}(n_\parallel)$ is the transmission coefficient of the layered geometry, relevant to the interface between medium 2 and medium 1. The normalized wavevector of the generic transmitted spectral plane wave inside (11) is $\mathbf{n}^{\rm t} = -\sqrt{1-(n_2 n_\parallel/n_1)^2}\hat{\mathbf{x}} + (n_2 n_\parallel/n_1)\hat{\mathbf{z}}$, derived from the Snell's law.

Using (11), the scattered-transmitted field is derived as follows:

$$V_{\rm st}^1(\xi,\zeta) = V_0 \sum_{\rm q=1}^{N} \sum_{\rm m=-\infty}^{+\infty} c_{\rm qm} \mathrm{TW_m^1}(\xi,\zeta;\chi_{\rm q}). \tag{12}$$

Beyond the latter field contribution, a scattered-reflected field does propagate in medium 1. It is a down-propagating contribution, arousing from multiple reflections of the field through the layer, as follows:

$$\mathrm{RW_m^1}(\xi,\zeta;\chi_{\rm q},\Lambda) = \frac{1}{2\pi}\int_{-\infty}^{+\infty} T_{21}(n_\parallel)\Gamma_{10}(n_\parallel) \times F_{\rm m}[-n_2(\chi_{\rm q} - \Lambda), n_\parallel] \times e^{in_1\sqrt{1-(n_2 n_\parallel/n_1)^2}(\xi+\Lambda)} e^{in_\parallel(\zeta-\eta_{\rm q})} dn_\parallel \tag{13}$$

where $\Gamma_{10}(n_\parallel)$ is the reflection coefficient, accounting for the interface between medium 1 and air, the top medium. The normalized wavevector of each plane wave is $\mathbf{n}^{\rm r} = \sqrt{1-(n_2 n_\parallel/n_1)^2}\hat{\mathbf{x}} + (n_2 n_\parallel/n_1)\hat{\mathbf{z}}$. Using (13) as basis functions, the scattered-reflected field $V_{\rm sr}^1$ is defined as follows:

$$V_{\rm sr}^1(\xi,\zeta) = V_0 \sum_{\rm q=1}^{N} \sum_{\rm m=-\infty}^{+\infty} c_{\rm qm} \mathrm{RW_m^{(1)}}(\xi,\zeta;\chi_{\rm q},\Lambda). \tag{14}$$

Finally, the scattered field reaches medium 0, after transmission through the layer. Transmitted cylindrical functions in medium 0, relevant to transmission at the interface in $\xi = 0$, are defined as follows:

$$\mathrm{TW_m^0}(\xi,\zeta;\chi) = \frac{1}{2\pi}\int_{-\infty}^{+\infty} T_{10}(n_\parallel) T_{21}(n_\parallel) \times F_{\rm m}[-n_2(\chi_{\rm q} - \Lambda), n_\parallel] \times e^{-i\sqrt{1-(n_2 n_\parallel)^2}\xi} e^{in_2 n_\parallel(\zeta-\eta_{\rm q})} dn_\parallel \tag{15}$$

with $T_{10}(n_\parallel)$ being the transmission coefficient, relevant to the interface between medium 1 and air. In (15), the normalized wavevector of the generic spectral component is $n^{\rm t} = -\sqrt{1-(n_2 n_\parallel)^2}\hat{\mathbf{x}} + n_2 n_\parallel \hat{\mathbf{z}}$. Using (15), the scattered transmitted field in medium 0 is found, as follows:

$$V_{\rm st}^0(\xi,\zeta) = V_0 \sum_{\rm q=1}^{N} \sum_{\rm m=-\infty}^{+\infty} c_{\rm qm} \mathrm{TW_m^0}(\xi,\zeta;\chi_{\rm q}). \tag{16}$$

In the above equations, fields are expressed in a rectangular frame. The unknown expansion coefficients $c_{\rm qm}$ of the scattered fields are found imposing boundary conditions on the cylinders' surface and deriving a linear system. Boundary conditions on the planar interfaces already tackled by the Fresnel reflection and transmission coefficients. Continuity of tangential fields on the cylinder surface can be imposed in an easier way if the involved fields in medium 2 are given in a reference frame centered on the axis of the pth scatterer, expressed in polar coordi-

nates. Transformation from rectangular to polar coordinates has to be performed on the transmitted plane wave in medium 2, and on the scattered field and the scattered-reflected field in medium 2. It is done expanding a plane wave in a series of Bessel functions $J_{\rm m}$.

As to the transmitted plane wave $V_{\rm t2}$, turning (5) in reference frames $\mathrm{RF_p}$, expressed in polar coordinates, leads to [20]

$$V_{\rm t2}(\xi,\zeta) = V_0 T_{01}(n_\parallel^{\rm i}) T_{12}(n_\parallel^{\rm i}) \times e^{in_2[n_\perp^{\rm t2}(\chi_{\rm p}-\Lambda)+n_\parallel^{\rm t2}\eta_{\rm p}]} \sum_{\ell=-\infty}^{+\infty} i^\ell J_\ell(n_2\rho_{\rm p}) e^{i\ell\theta_{\rm p}} e^{-i\ell\varphi_{\rm t2}}. \quad (17)$$

As to the scattered field $V_{\rm s}$ in (6), it is written in a form stressing the interaction of the wave radiated by the qth cylinder with the remaining p cylinders, making use of the addition theorem of Hankel functions [26]

$$H_{\rm m}^{(1)}(n_2\rho_{\rm q}) e^{i{\rm m}\theta_{\rm q}} = e^{i{\rm m}\theta_{\rm qp}} \sum_{\ell=-\infty}^{+\infty} i^{-\ell} H_{{\rm m}+\ell}^{(1)}(n_2\rho_{\rm qp}) \times e^{i\ell\theta_{\rm qp}} J_\ell(n_2\rho_{\rm p}) e^{-i\ell\theta_{\rm p}}. \quad (18)$$

The transformation equation (18) allows to center the general cylindrical wave emitted by the q-th cylinder in the $\mathrm{RF_p}$ system. The final expression of the field $V_{\rm s}$ in polar coordinates is [20]

$$V_{\rm s}(\xi,\zeta) = V_0 \sum_{\ell=-\infty}^{+\infty} J_\ell(n_2\rho_{\rm p}) e^{i\ell\theta_{\rm p}} \sum_{\rm q=1}^{N} \sum_{\rm m=-\infty}^{+\infty} c_{\rm qm} \times \left[{\rm CW}_{{\rm m}-\ell}(n_2\xi_{\rm qp}, n_2\zeta_{\rm qp})(1-\delta_{\rm qp}) + \frac{H_\ell^{(1)}(n_2\rho_{\rm p})}{J_\ell(n_2\rho_{\rm p})} \delta_{\rm qp}\delta_{\ell{\rm m}} \right] \quad (19)$$

where $\delta_{\rm qp}$ and $\delta_{\ell{\rm m}}$ are the Kronecker symbols. Finally, the expression of scattered-reflected field $V_{\rm sr}$ (10) in reference frames $\mathrm{RF_p}$, expressed in polar coordinates, is

$$V_{\rm sr}(\xi,\zeta) = V_0 \sum_{\ell=-\infty}^{+\infty} J_\ell(n_2\rho_{\rm p}) e^{i\ell\theta_{\rm p}} \sum_{\rm q=1}^{N} \sum_{\rm m=-\infty}^{+\infty} c_{\rm qm} \times {\rm RW}_{{\rm m}+\ell}[-n_2(\chi_{\rm p}+\chi_{\rm q}-2\Lambda), n_2(\eta_{\rm p}-\eta_{\rm q})]. \quad (20)$$

Now boundary conditions on the cylinders' surface for the fields propagating in medium 2 are imposed, i.e., zero tangential electric field. For the TM- and TE-polarization, we have the two following equations, respectively:

$$\left[V_{\rm t2}+V_{\rm s}+V_{\rm sr} \right]_{\rho_{\rm p}=k_0\alpha_{\rm p}} = 0, \quad \text{with } {\rm p}=1,...,N \quad (21)$$

$$\left[\frac{\partial}{\partial\rho_{\rm p}}(V_{\rm t2}+V_{\rm s}+V_{\rm sr}) \right]_{\rho_{\rm p}=k_0\alpha_{\rm p}} = 0, \quad \text{with } {\rm p}=1,...,N. \quad (22)$$

Substituting in (21) and (22), (17), (19), and (20), and using the property of orthogonality satisfied by exponential functions, after some algebra, it is possible to derive a linear system in the unknown coefficients $c_{\rm qm}$, as follows:

$$\sum_{\rm q=1}^{N} \sum_{\rm m=-\infty}^{+\infty} A_{{\rm m}\ell}^{{\rm qp(TM,TE)}} c_{\rm qm} = B_\ell^{\rm p(TM,TE)} \times \begin{cases} \ell = 0, \pm1, \ldots, \pm\infty \\ {\rm p} = 1, \ldots, N \end{cases} \quad (23)$$

with

$$A_{{\rm m}\ell}^{\rm qp(TM,TE)} = i^{-\ell} G_\ell^{\rm (TM,TE)} \Big\{ {\rm CW}_{{\rm m}-\ell}(n_2\xi_{\rm qp}, n_2\zeta_{\rm qp}) \times (1-\delta_{\rm qp}) + \frac{\delta_{\rm qp}\delta_{\ell{\rm m}}}{G_\ell^{\rm (TM,TE)}(n_2\rho_{\rm p})} + {\rm RW}_{{\rm m}+\ell}[-n_2(\chi_{\rm p}+\chi_{\rm q}-2\Lambda), n_2(\eta_{\rm p}-\eta_{\rm q})] \Big\} \quad (24)$$

$$B_\ell^{\rm p(TM,TE)} = -G_\ell^{(TM,TE)} \Big\{ T_{10}(n_\parallel^{\rm i}) T_{21}(n_\parallel^{\rm i}) \times e^{in_1[n_\perp^{\rm t1}(\chi_{\rm p}-\Lambda)+n_\parallel^{\rm t1}\eta_{\rm p}]} e^{-i\ell\varphi^{\rm t1}} \Big\} \quad (25)$$

where $G_\ell^{\rm (TM)}(x)=J_\ell(x)/H_\ell^{(1)}(x)$ and $G_\ell^{\rm (TE)}=J_\ell'(x)/H_\ell'^{(1)}(x)$.

III. Numerical Implementation and Results

For the numerical implementation of the theory presented in Section II, the cylindrical functions employed to expand the scattered-field contributions have been evaluated in an accurate way, applying the algorithm developed in the frame of the CWA [22]. The fundamentals of the algorithm are in a decomposition of the integration domain into subintervals, according to the evanescent or homogeneous behavior of the plane waves of the spectrum. On these subintervals, Gaussian rules or low-order Legendre quadrature formulas have been used for the integration, together with adaptive techniques to implement further decompositions of the integration algorithms with the highly oscillating kernels of the homogeneous parts. Therefore, the code allows an accurate evaluation of the scattered fields both in the near- and far-field zone. Moreover, the system derived in (23) has to be solved in order to obtain the expansion coefficients of the scattered-field contributions and compute the total scattered field in each point $P(\xi,\zeta)$ of the space. The rule $M = 3n_1\alpha$ [27] has been used for a truncation on the order m relevant to the expansion into cylindrical waves in (23). The resulting system order is $N = 2M + 1$, with a computational cost that is identical to the one obtained in a semi-infinite medium. Each element of the matrix corresponds to the computation of two scattered fields, i.e., the scattered field $V_{\rm s}$ (19) and the scattered-reflected field $V_{\rm sr}$ (20). The computational cost can be compared with the one in the multiple-reflection approach used in [20] for the same geometrical layout presented in this paper. In [20], the system order is $N = 2M + 1$, but each matrix element requires the evaluation of a higher number of terms. In particular, beyond the scattered-field $V_{\rm s}$ and the scattered-reflected field $V_{\rm sr}$,

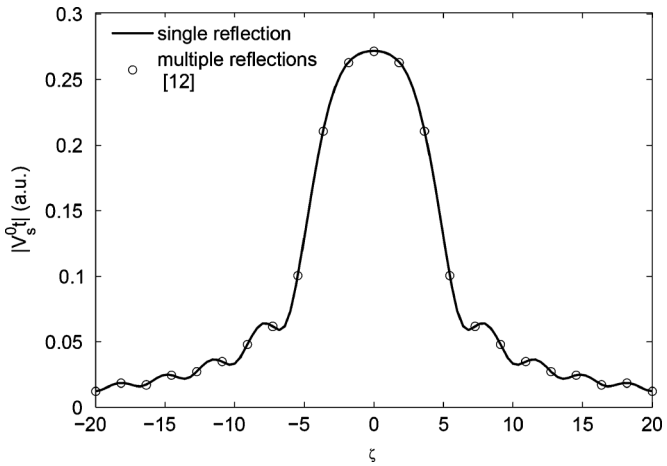

Fig. 4. Scattered field along a line in $\xi = -0.1$, with $\alpha = 1$, $\chi = 5$, $\Lambda = 1$ $\varepsilon_{r1} = 2.25$, $\varepsilon_{r2} = 9$, $\varphi_i = 0$, TM-polarization—comparison between CWA with single-reflection approach and multiple-reflection approach [20] with $R = 6$ reflections.

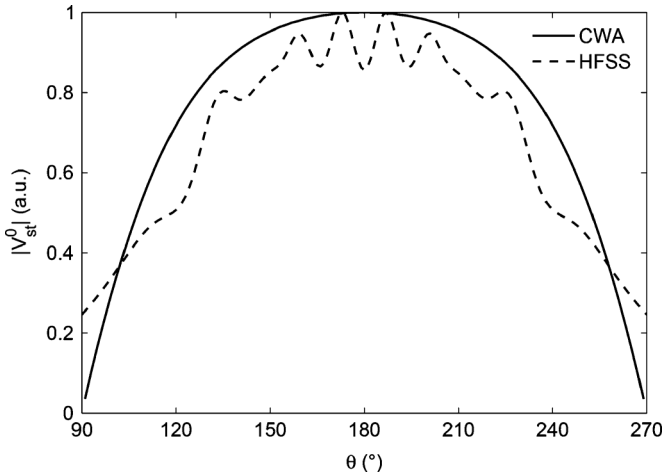

Fig. 5. Far-field scattering with $a = 5$ cm, $\chi = 80$ cm, $\Lambda = 20$ cm $\varepsilon_{r1} = 4$, $\varepsilon_{r2} = 5$, $\varphi_i = 0$, TM-polarization—comparison between CWA with single-reflection approach and Ansys HFSS [28] simulation.

a scattered-reflected-transmitted field $V_{\mathrm{str}(j)}$ has to be evaluated that takes into account the infinite number of reflections $j = 1, 2, \ldots$ occurring inside the slab. Such number of reflections is truncated in the numerical implementation to a finite number $j = 1, 2, \ldots, R$, according to a criterion of accuracy in the results. In particular, the multiple-reflection code is run in an iterative way, starting from $R = 1$ reflection, and increasing R at the end of each iteration. The code execution is stopped when an accuracy of at least 10^{-2} is achieved on the magnitude of the scattered field at two consecutive iterations.

In Fig. 4, the scattered-trasmitted field in air V_t^0 is evaluated along a line in $\xi = -0.1$, parallel to the interface. A wall of normalized thickness $\Lambda = 1$ and relative permittivity $\varepsilon_{r1} = 2.25$, and a buried perfectly conducting cylinder with normalized radius $\alpha = 1$, placed at a depth $\chi = 5$, in a medium of permittivity $\varepsilon_{r2} = 9$, have been simulated. The excitation is a plane-wave in normal incidence ($\varphi_i = 0$), and in TM polarization. Results obtained with the proposed single-reflection technique are also compared with the results from the iterative method presented in [20], showing the perfect agreement of the improved technique with the previous approach. In Table I, the estimated computer time for the computation of the scattered field in the plots in Fig. 4, evaluated on 100 points along the ζ-axis, on an Intel Xeon CPU E5420 @2.5 GHz, RAM 16 GB, are reported, for different values of the cylinder radius. It can be pointed out that the field maps in the following Figs. 6–10 are obtained evaluating the scattered field in a rectangular grid of 200×200 points in order to obtain high-quality maps. It is clear that, with the new single-reflection approach, an effective reduction of the execution times is entailed, especially when the field is evaluated on a large spatial domain.

A comparison of the method with results from a commercial software has been also performed, with satisfactory agreement. In Fig. 5, the far-field scattering from the single reflection approach with CWA and from Ansys HFSS [28] is reported. A cylinder of radius $a = 5$ cm, with center buried at a depth of 80 cm from the air–medium 1 interface has been simulated. Layer thickness is $\Lambda = 20$ cm, and the relative permittivities of the media are $\varepsilon_{r1} = 4$ and $\varepsilon_{r2} = 5$. The source field is in

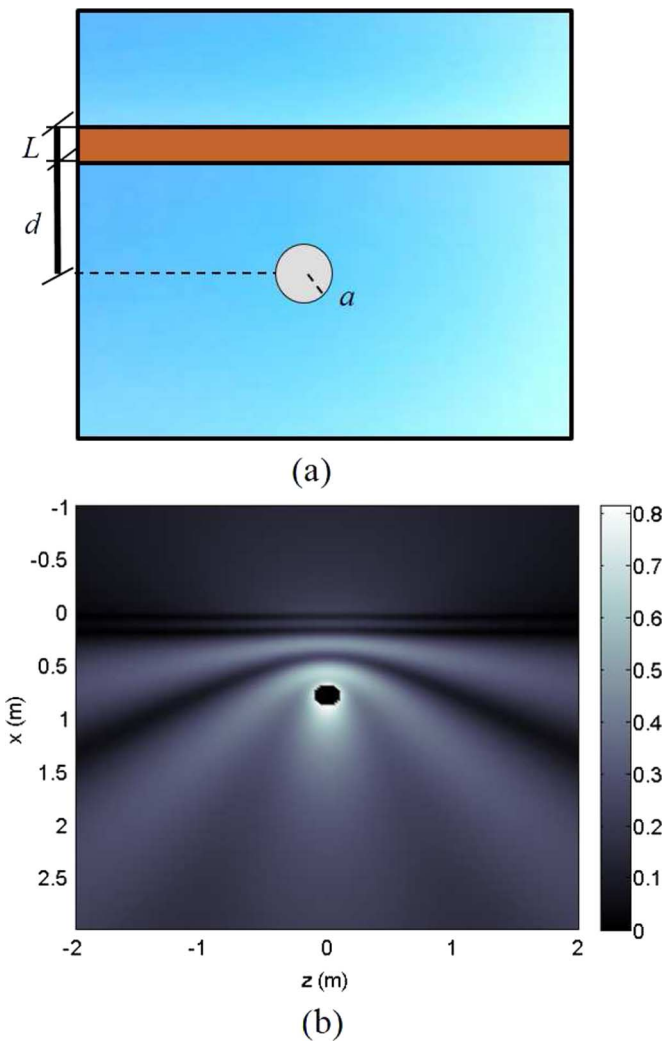

Fig. 6. Through-wall scattering by a cylinder below a brick wall ($\varepsilon_{r1} = 4$): (a) geometry of the problem; (b) magnitude of the total scattered field with $a = 5$ cm, $L = 20$ cm, $d = 60$ cm, normal incidence ($\varphi_i = 0$), and $f = 600$ MHz.

normal incidence ($\varphi_i = 0$) and polarization is TM. In Ansys HFSS, the 2D unbounded domain solved by the CWA has been turned into a 3D one with small thickness along the y-direction.

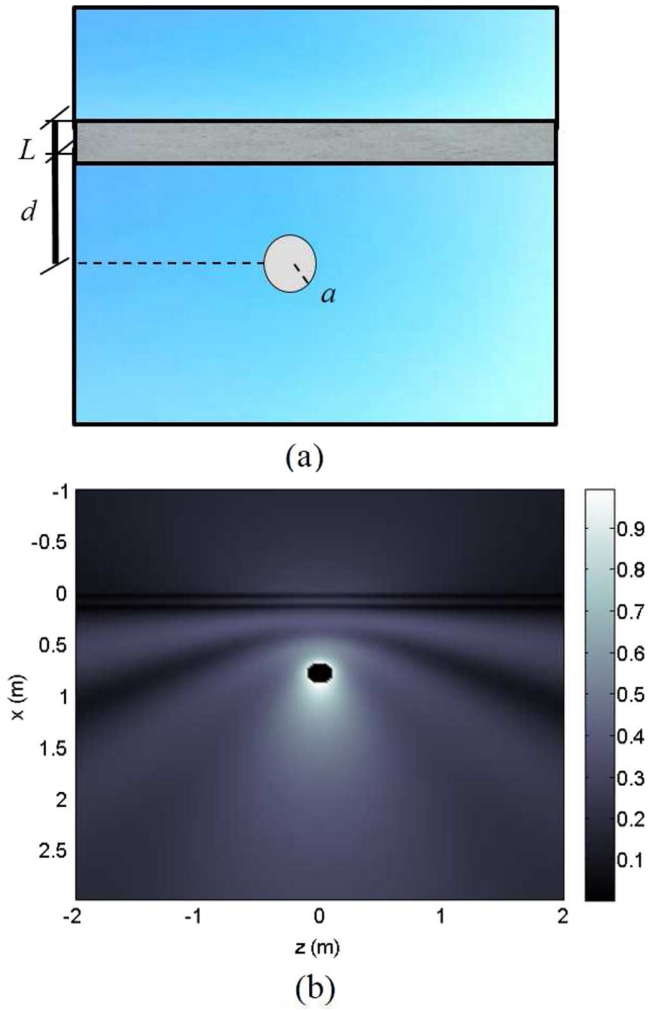

Fig. 7. Through-wall scattering by a cylinder below a concrete wall ($\varepsilon_{r1} = 6$): (a) geometry of the problem; (b) magnitude of the total scattered field with $a =$ 5 cm, $L = 20$ cm, $d = 60$ cm, normal incidence ($\varphi_i = 0$), and $f = 600$ MHz.

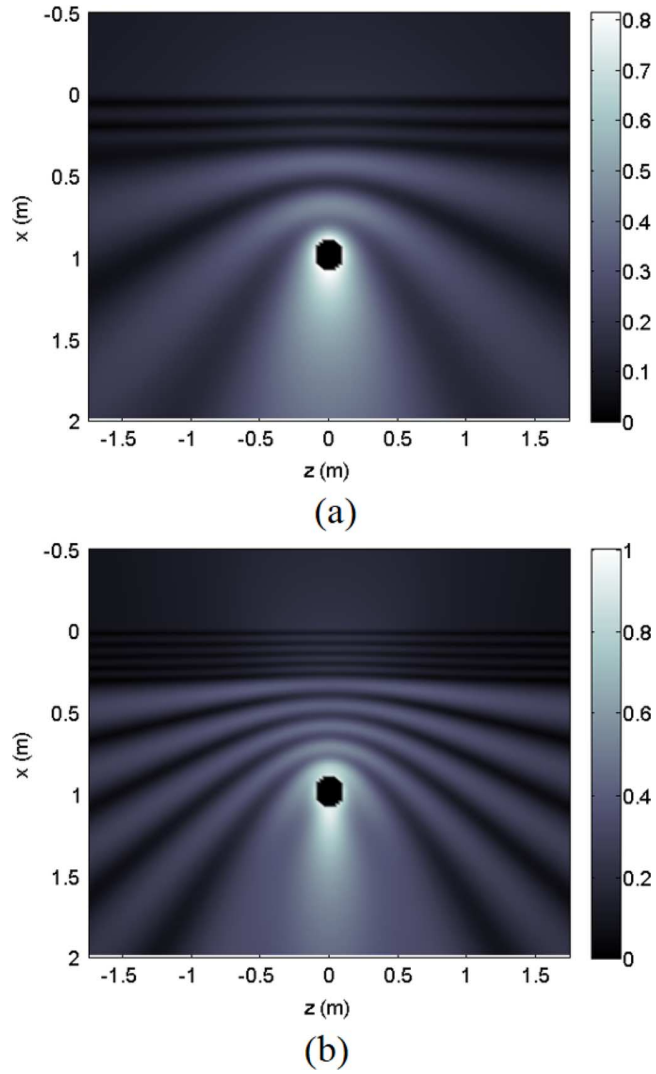

Fig. 8. Magnitude of the total scattered field in through-wall scattering by a cylinder below a brick wall ($\varepsilon_{r1} = 4$), with $a = 10$ cm, $L = 20$ cm, $d = 70$ cm, normal incidence ($\varphi_i = 0$): (a) $f = 600$ MHz and (b) $f = 1200$ MHz.

Absorbing boundary conditions and layered impedance boundaries have been assigned at the edges of the x- and z-directions, whereas master and slave boundaries have been enforced along the z-axis. Results from the two methods are normalized to their maximum value.

In Tables II–IV, dependence of execution times on other simulation parameters is further explored. Times are still obtained evaluating the scattered field on 100 points along the ζ-axis, along a line in $\xi = -0.1$; for the considered cases, the incident field is normally impinging and in TM-polarization. In Table II, the effect of the permittivity of the layer is analyzed, with four values $\varepsilon_{r1} = 4, 9, 25, 49$. The other simulation parameters are $\alpha = 1$, $\chi = 5$, $\Lambda = 1$, and $\varepsilon_{r1} = 2.25$. With both the approaches, execution times get longer as the permittivity of the layer is increased. Anyway, for a fixed value of ε_{r1}, the difference between the two methods is of almost two orders of magnitude.

The effect of the layer thickness Λ on the execution time is highlighted in Table III, for a scattering problem with $\alpha = 1$, $\chi = 20$, $\varepsilon_{r1} = 9$, and $\varepsilon_{r2} = 2.25$. Execution time turns out not to be heavily affected by the layer thickness. As Λ is increased, keeping fixed the medium permittivity, execution time gets faster. This is particularly true for the multiple reflection approach: with an increase in the layer thickness, multiple reflection fields propagate along a longer path and are rapidly attenuated. Therefore, a lower number of reflections R is needed to reach field convergence.

The role of the number of cylinders N included in the simulation is shown in Table IV. Cylinders have identical radii $\alpha_q = 1$ ($q = 1, \ldots, N$) and are placed at a fixed depth $\chi_q = 5$, below a layer of thickness $\Lambda = 1$. Relative permittivities of the media are $\varepsilon_{r1} = 2.25$, and $\varepsilon_{r2} = 9$. Results of execution time for the scattering from one cylinder ($N = 1$) are compared with the ones from a number of cylinders $N > 1$, i.e., $N = 3, 5, 10$. The distance between the cylinders' axis is $\Delta = 5$. Simulation time is very sensitive to this parameter. Even in the noniterative approach, results from 1 to 10 cylinders differ more than an order of magnitude. Anyway, from the comparisons with the multiple reflection approach, where execution time is heavily longer, the novel method turns out to be highly efficient.

An application of the method described in Section II is the simulation of through-wall scattering scenarios, i.e., of targets hidden by a masonry wall. Imaging of building interiors has in

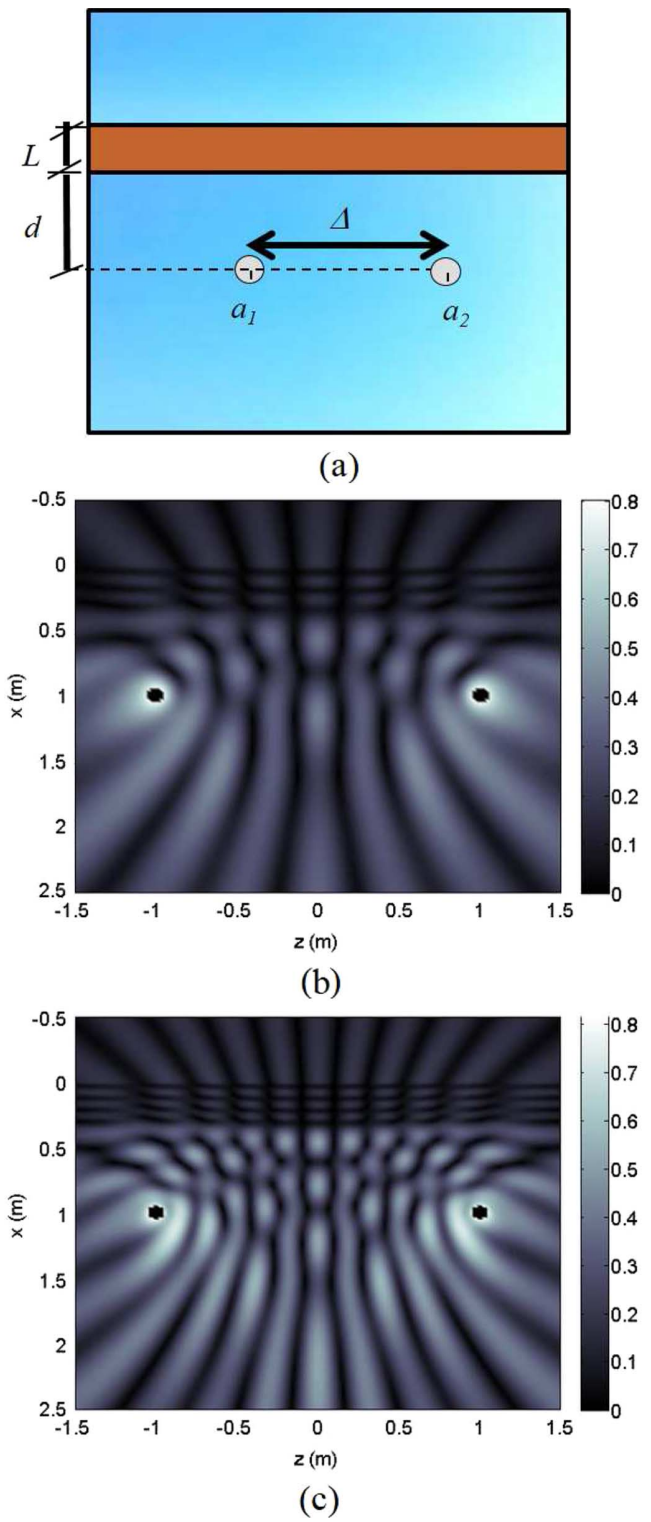

Fig. 9. Through-wall scattering by two cylinders below a brick wall ($\varepsilon_{r1} = 4$), with $a_1 = a_2 = 10$ cm, $\Delta = 2$ m, $L = 30$ cm, $d = 70$ cm, normal incidence ($\varphi_i = 0$): (a) geometry of the problem and (b) magnitude of the total scattered field at $f = 600$ MHz; (c) magnitude of the total scattered field at $f = 1200$ MHz.

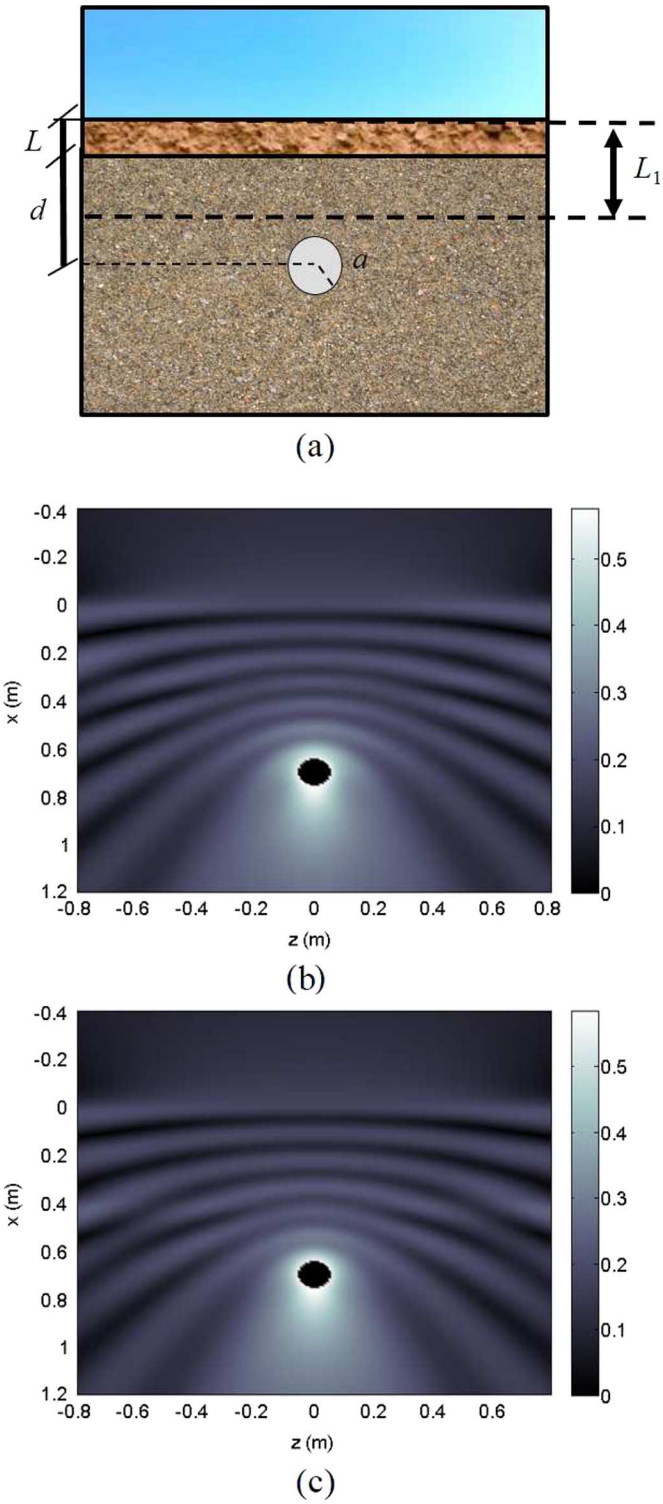

Fig. 10. Scattering by a buried metallic pipe in ground of permittivity $\varepsilon_{r2} = 7$, below a soil of different permittivity $\varepsilon_{r1} = 5$, with $d = 70$ cm, $a = 5$ cm, $f = 600$ MHz, normal incidence ($\varphi_i = 0$), and TM-polarization: (a) geometry of the problem and (b) magnitude of the total scattered field with $L = 10$ cm; and (c) magnitude of the total scattered field with $L_1 = 40$ cm.

general wide applications in contexts of security and surveillance. The electromagnetic modeling of through-wall problems is a useful tool in the development of efficient techniques of through-wall imaging. The 2D electromagnetic modeling can be implemented dividing the entire space into three media, with two external half-spaces filled by air, and a central layer with the relative permittivity of the wall material. The source is in the top half-space, whereas the targets of the imaging reconstruction are placed in the lowest one, hidden by the wall. With the

TABLE I
COMPARISON BETWEEN THE EXECUTION TIMES FOR THE SINGLE-REFLECTION APPROACH AND THE MULTIPLE REFLECTION APPROACH IN [20] FOR THE SCATTERED-FIELD PLOTS IN FIG. 4, FOR DIFFERENT VALUES OF THE CYLINDER RADIUS

	single reflection	multiple reflections	
radius	execution time [sec]	execution time [sec]	R #reflections
$\alpha = 1$	2.89	125.38	6
$\alpha = 2$	6.17	252.40	6
$\alpha = 3$	10.48	392.68	6

TABLE II
COMPARISON BETWEEN THE EXECUTION TIMES FOR THE SINGLE-REFLECTION APPROACH AND THE MULTIPLE REFLECTION APPROACH IN [20], FOR DIFFERENT VALUES OF THE REFRACTION INDEX OF MEDIUM 1 ($\alpha = 1$, $\chi = 5$, $\Lambda = 1$, $\varepsilon_{\mathrm{r}2} = 2.25$, $\varphi_i = 0$, TM-POLARIZATION, SCATTERED FIELD ALONG A LINE IN $\xi = -0.1$)

	single reflection	multiple reflections	
medium 1	execution time [sec]	execution time [sec]	R #reflections
$\varepsilon_{\mathrm{r}1} = 4$	1.42	75.84	6
$\varepsilon_{\mathrm{r}1} = 9$	2.34	252.40	12
$\varepsilon_{\mathrm{r}1} = 25$	4.34	392.68	8
$\varepsilon_{\mathrm{r}1} = 49$	6.69	595.28	8

TABLE III
COMPARISON BETWEEN THE EXECUTION TIMES FOR THE SINGLE-REFLECTION APPROACH AND THE MULTIPLE REFLECTION APPROACH IN [20], FOR DIFFERENT VALUES OF THE LAYER THICKNESS ($\alpha = 1$, $\chi = 20$, $\varepsilon_{\mathrm{r}1} = 9$, $\varepsilon_{\mathrm{r}2} = 2.25$, $\varphi_i = 0$, TM-POLARIZATION, SCATTERED FIELD ALONG A LINE IN $\xi = -0.1$)

	single reflection	multiple reflections	
layer thickness	execution time [sec]	execution time [sec]	R #reflections
$\Lambda = 0.1$	2.11	127.88	6
$\Lambda = 0.5$	2.10	70.62	4
$\Lambda = 5$	1.86	69.72	4
$\Lambda = 15$	1.71	67.66	4

TABLE IV
COMPARISON BETWEEN THE EXECUTION TIMES FOR THE SINGLE-REFLECTION APPROACH AND THE MULTIPLE REFLECTION APPROACH IN [20], FOR DIFFERENT VALUES OF THE NUMBER OF CYLINDERS ($\alpha_{\mathrm{q}} = 1$, $\chi_{\mathrm{q}} = 5$, $\Lambda = 1$, $\varepsilon_{\mathrm{r}1} = 2.25$, $\varepsilon_{\mathrm{r}2} = 9$, $\Delta = 5$, $\varphi_i = 0$, TM-POLARIZATION, SCATTERED FIELD ALONG A LINE IN $\xi = -0.1$)

	single reflection	multiple reflections	
number of cylinders	execution time [sec]	execution time [sec]	R #reflections
$N = 1$	2.89	125.38	6
$N = 3$	9.26	381.60	6
$N = 5$	16.59	1024.72	8
$N = 10$	44.75	3326.32	10

proposed scattering technique, the imaging problem can be simulated putting $\varepsilon_{\mathrm{r}2} = 1$ for the relative permittivity of medium 2, and choosing the desired value for the permittivity of the wall. One or more scatterers can be arbitrarily placed below the wall.

A first example of through-wall geometry is reported in Fig. 6(a). A perfectly conducting cylinder of radius $a = 5$ cm is placed in an air-filled medium ($\varepsilon_{\mathrm{r}2} = 1$), below a brick wall simulated with a homogeneous layer of relative permittivity $\varepsilon_{\mathrm{r}1} = 4$, and thickness $L = 20$ cm, at a distance from the wall $d = 60$ cm. The incident field is a plane wave in normal incidence ($\varphi_i = 0$) and in TM-polarization. The magnitude of the scattered field is reported in Fig. 6(b) in a two-dimensional field map, evaluated at a frequency of 600 MHz. The same through-wall scenario is considered in Fig. 7(a) for a wall of concrete, simulated with a permittivity $\varepsilon_{\mathrm{r}1} = 6$. In Fig. 7(b), the scattered field below the wall is higher compared with the one in Fig. 6(b), due to the different wall permittivity. In both Figs. 6(b) and 7(b), the wall can be distinguished from the two half-spaces, due to the pronounced fringes of interference of the field extending over its width. A thicker brick wall with $L = 20$ cm is considered in Fig. 8, for excitation by a plane wave in normal incidence ($\varphi_i = 0$) and in TM-polarization. A perfectly conducting cylinder of radius $a = 10$ cm is buried at a distance $d = 70$ cm from the wall. In Fig. 8(a), the magnitude of the scattered field is evaluated at $f = 600$ MHz. This figure can be compared with Fig. 8(b), evaluated at a doubled frequency of 1200 MHz. A visible doubling of the fringes of interference of the field in both the wall and the lowest medium occurs, accounting for the doubled frequency of analysis.

A case of two hidden targets is simulated in Fig. 9. The targets are two circular cross-section cylinders with equal radii $a_1 = a_2 = 10$ cm, distance $\Delta = 2$ m between their centers, and placed at $d = 70$ cm from the bottom boundary of the layer [Fig. 9(a)]. The dielectric layer models a brick wall of thickness $L = 30$ cm; the incident field is a plane wave in normal incidence and TM-polarization. The magnitude of the total scattered field is evaluated at two frequencies: $f = 600$ MHz in Fig. 9(b) and $f = 1200$ MHz in Fig. 9(c). Considering in medium 0 ($\xi < 0$) a line parallel to the interface, the scattered field has several nulls, depending on the chosen wavelength of analysis. The number of nulls is increased as the wavelength is decreased, as it is clear from a comparison between the two figures.

The general theory developed in Section II is also suitable to simulate a stack of three media, where the last half-space (medium 2) is filled by an arbitrary permittivity for geophysical applications. An example of a possible simulation layout is depicted in Fig. 10(a), where a metallic pipe of radius $a = 5.5$ cm, simulating a buried service, is placed in a soil of relative permittivity $\varepsilon_{\mathrm{r}2} = 7$ after a layer filled by a soil with different permittivity $\varepsilon_{\mathrm{r}1} = 5$; the distance of the center of the pipe from the lowest boundary of the layer is $d = 70$ cm. The two-dimensional field map for a soil of thickness $L = 10$ cm is given in Fig. 10(b). Keeping the pipe at a fixed depth, the layout in Fig. 10(a) is simulated also for an increased thickness of the soil layer of $L_1 = 40$ cm, and the relevant field map is given in Fig. 10(c). In both Fig. 10(b) and (c), the presence of the layer is not visible, as the field map has a continuous intensity profile across the layer and the lower medium, i.e., in the space $\xi > 0$. Medium 1 and medium 2 are stacked with an increasing value of permittivity, i.e., $n_1 < n_2$, whereas in the previous layouts of through-wall, simulated in Figs. 6–9, it is $n_1 > n_2$. This has a strong effect of interference inside medium 1, which makes the layer clearly distinguishable from the lower medium.

IV. CONCLUSION

A technique for a fast computation of the field scattered by cylinders placed below a dielectric layer has been presented, based on the CWA. Through suitable reflection and transmission coefficients used inside plane-wave spectra, the interaction of the scattered field with the two interfaces bounding the layer has been evaluated with a single-reflection scheme. The numerical implementation of the method has proved its validity,

through a comparison with results from a multiple-reflection approach, also demonstrating its advantage in terms of reduced computational times. Numerical results have shown how the developed technique is particularly suitable for the simulation of through-wall scenarios. Applications are also possible in the frame of the geophysical modeling of a layered ground. A future extension of the work will be a layout with scatterers placed below a stratified medium.

REFERENCES

[1] D. J. Daniels, *Surface Penetrating Radar*, 2nd ed. London, U.K.: IEE, 2004.

[2] *Through-the-Wall Radar Imaging*, M. G. Amin, Ed. Boca Raton, FL, USA: CRC Press, 2010.

[3] E. J. Baranoski, "Through wall imaging: Historical perspective and future directions," in *Proc. IEEE Int. Conf. Acoust., Speech, Signal Process. (ICASSP)*, 2008, pp. 5173–5176.

[4] A. Kusiek and J. Mazur, "Analysis of scattering from arbitrary configuration of cylindrical objects using hybrid finite-difference mode-matching method," *Progr. Electromagn. Res.*, vol. 97, pp. 105–127, 2009.

[5] A. Kusiek and J. Mazur, "Hybrid finite-difference/mode-matching method for analysis of scattering from arbitrary configuration of rotationally-symmetrical posts," *Progr. Electromagn. Res.*, vol. 110, pp. 23–42, 2010.

[6] A. Kusiek and J. Mazur, "Hybrid technique for the analysis of scattering from periodic structures composed of irregular objects," *Progr. Electromagn. Res.*, vol. 135, pp. 657–675, 2013.

[7] H. Jia and K. Yasumoto, "Scatteration and absorption characteristics of multilayered gratings embedded in a dielectric slab," *Int. J. Infrared Millim. Wave*, vol. 26, no. 8, pp. 1111–1126, Aug. 2005.

[8] S. C. Lee, "Light scattering by closely spaced parallel cylinders embedded in a finite dielectric slab," *J. Opt. Soc. Amer. A*, vol. 16, no. 6, pp. 1350–1361, June 1999.

[9] R. Paknys, "Reflection and transmission by reinforced concrete-numerical and asymptotic analysis," *IEEE Trans. Antennas Propag.*, vol. 51, no. 10, pp. 2852–2861, Oct. 2003.

[10] F. Frezza, L. Pajewski, C. Ponti, and G. Schettini, "Scattering by perfectly conducting circular cylinders buried in a dielectric slab through the cylindrical wave approach," *IEEE Trans. Antennas Propag.*, vol. 57, pp. 1208–1217, Apr. 2009.

[11] F. Frezza, L. Pajewski, C. Ponti, and G. Schettini, "Scattering by dielectric circular cylinders in a dielectric slab," *J. Opt. Soc. Amer. A*, vol. 27, pp. 687–695, 2010.

[12] K. A. Michalski and D. Zheng, "Electromagnetic scattering and radiation by surfaces of arbitrary shape in layered media, Part I: Theory," *IEEE Trans. Antennas Propag.*, vol. 38, no. 3, pp. 335–344, Mar. 1990.

[13] K. A. Michalski and D. Zheng, "Electromagnetic scattering and radiation by surfaces of arbitrary shape in layered media, Part II: Implementation and results for contiguous half-spaces," *IEEE Trans. Antennas Propag.*, vol. 38, no. 3, pp. 345–352, Mar. 1990.

[14] J. L. Tsalamengas, "Electromagnetic scattering from conducting circular cylinders in the presence of a stratified anisotropic medium," *IEEE Trans. Antennas Propag.*, vol. 37, no. 12, pp. 1582–1590, Apr. 1989.

[15] F. Soldovieri and R. Solimene, "Through-wall imaging via a linear inverse scattering algorithm," *Geosc. Remote Sens. Lett.*, vol. 4, no. 4, pp. 513–517, 2007.

[16] A. Giannopoulos, "Modelling ground penetrating radar by GprMax," *Constr. Build. Mater.*, vol. 19, pp. 755–762, 2005.

[17] C. Lei and S. Ouyang, "Through-wall surveillance using ultra-wideband short pulse radar: Numerical simulation," in *Proc. 2nd IEEE Int. Conf. Ind. Electron. Appl.*, 2007, pp. 1551–1554.

[18] M. Dehmollaian and K. Sarabandi, "Hybrid FDTD and ray optics approximation for simulation of through-wall microwave imaging," in *Proc. Antennas Propag. Soc. Int. Symp.*, 2006, pp. 249–252.

[19] P. C. Chang, R. J. Burkholder, J. L. Volakis, R. J. Marhefka, and Y. Bayram, "High-frequency EM characterization of through-wall building imaging," *IEEE Trans. Geosci. Remote Sens.*, vol. 47, no. 5, pp. 1375–1387, 2009.

[20] F. Frezza, L. Pajewski, C. Ponti, and G. Schettini, "Through-wall electromagnetic scattering by N conducting cylinders," *J. Opt. Soc. Amer. A*, vol. 30, no. 8, pp. 1632–1639, Aug. 2013.

[21] M. Di Vico, F. Frezza, L. Pajewski, and G. Schettini, "Scattering by a finite set of perfectly conducting cylinders buried in a dielectric half-space: A spectral-domain solution," *IEEE Trans. Antennas Propag.*, vol. 53, no. 2, pp. 719–727, Feb. 2005.

[22] M. Di Vico, F. Frezza, L. Pajewski, and G. Schettini, "Scattering by buried dielectric cylindrical structures," *Radio Sci.*, vol. 40, no. RS6S18, 2005.

[23] M. A. Fiaz, F. Frezza, L. Pajewski, C. Ponti, and G. Schettini, "Scattering by a circular cylinder buried under a slightly rough surface: The cylindrical-wave approach," *IEEE Trans. Antennas Propag.*, vol. 60, pp. 2834–2842, Jun. 2012.

[24] M. A. Fiaz, C. Ponti, and G. Schettini, "On the scattering by a cylindrical object below a rough surface with the CWA," presented at the *IEEE MTT-S Int. Conf. Numer. Electromagn. Model. Optim. RF, Microw., THz Appl.*, Pavia, Italy, May 14–16, 2014.

[25] S. J. Orfanidis, *Electromagnetic Waves and Antennas*. Piscataway, NJ, USA: Rutgers Univ., 2014 [Online]. Available: http://eceweb1.rutgers.edu/~orfanidi/ewa/

[26] I. N. Sneddon, *Mixed Boundary Value Problems in Potential Theory*. Amsterdam, The Netherlands: North-Holland, 1966.

[27] A. Z. Elsherbeni, "A comparative study of two-dimensional multiple scattering techniques," *Radio Sci.*, vol. 29, pp. 1023–1033, 1994.

[28] ANSYS High Frequency Structure Simulator, Release 15.0 Ansys, Inc.

Cristina Ponti (M'11) received the *cum laude* First Level Laurea and the *cum laude* Laurea Magistralis in electronic engineering, from the Sapienza University of Rome, Italy, in February 2004 and February 2006, respectively, and the Ph.D. degree from Roma Tre University of Rome, Italy, in March 2010.

In the same year, she joined the Department of Engineering of Roma Tre University of Rome as an Assistant Researcher, and since December 2010, she has been an Assistant Professor in electromagnetic fields. Her main research interests are in electromagnetic theory, numerical methods, scattering by buried objects, electromagnetic band-gap (EBG) structures, antennas for microwave and millimeter applications, and nuclear fusion.

Dr. Ponti is a member of the IEEE Antennas and Propagation Society and Microwave Theory and Technique Society, of the Italian Elecromagnetic Society (SIEm), and of CNIT. She is actively involved in the Cost Action TU1208 Civil Engineering Applications of Ground Penetrating Radar, as a participant and as leader of the Project "Development of New Methods for the Solution of Forward Electromagnetic Scattering by Buried Objects.

Stefano Vellucci received the Laurea degree in electronic engineering from the "Roma Tre" University, Rome, Italy, in 2012, with a thesis on the realization of a metamaterial dual-band branch-line hybrid coupler.

He is currently working towards the Laurea Magistralis degree in electronic engineering at the "Roma Tre" University . His main interests are microwave components and scattering problems.